

## Research Article

# Numerical-Experimental Correlation of Interlaminar Damage Growth in Composite Structures: Setting Cohesive Zone Model Parameters

F. Di Caprio <sup>1</sup>, S. Saputo <sup>2</sup>, and A. Sellitto <sup>2</sup>

<sup>1</sup>Italian Aerospace Research Center (CIRA), via Maiorise Snc, Capua, CE 81043, Italy

<sup>2</sup>University of Campania “L. Vanvitelli”-Department of Engineering, Via Roma 29, Aversa, CE 81031, Italy

Correspondence should be addressed to S. Saputo; [salvatore.saputo@unicampania.it](mailto:salvatore.saputo@unicampania.it)

Received 14 May 2019; Revised 4 July 2019; Accepted 26 August 2019; Published 13 October 2019

Academic Editor: Lingxue Kong

Copyright © 2019 F. Di Caprio et al. This is an open access article distributed under the Creative Commons Attribution License, which permits unrestricted use, distribution, and reproduction in any medium, provided the original work is properly cited.

Composite laminates are characterized by high mechanical in-plane properties while experiencing, on the contrary, a poor out-of-plane response. The composite laminates, indeed, are often highly vulnerable to interlaminar damages, also called “delaminations.” One of the main techniques used for the numerical prediction of interlaminar damage onset and growth is the cohesive zone model (CZM). However, this approach is characterised by uncertainties in the definition of the parameters needed for the implementation of the cohesive behaviour in the numerical software. To overcome this issue, in the present paper, a numerical-experimental procedure for the calibration of material parameters governing the mechanical behaviour of CZM based on cohesive surface and cohesive element approaches is presented. Indeed, by comparing the results obtained from the double cantilever beam (DCB) and end-notched flexure (ENF) experimental tests with the corresponding numerical results, it has been possible to accurately calibrate the parameters of the numerical models needed to simulate the delamination growth phenomenon at coupon level.

## 1. Introduction

Despite their high mechanical properties and their low weight, compared to classic metallic alloys, composite material damage behaviour is difficult to predict and control. The characteristic damage mechanisms of composite materials can be catalogued in intralaminar damages (fibre and/or matrix failure) and interlaminar damages (delaminations) [1–4]. Among all the damage mechanisms, delaminations can propagate under service load, seriously reducing the carrying load capability of the overall structure [5, 6]. For this reason, the mechanical behaviour of composite structure with interlaminar damages has been widely investigated in the literature, both experimentally and numerically. In particular, fracture mechanic has been widely used to model interlaminar damage evolution through FE-based procedures such as virtual crack closure technique (VCCT) and cohesive zone model (CZM) theory [7–12]. Delamination growth forecasts, obtained with numerical models designed

on the VCCT basis, have shown that they are strongly dependent on the finite element size along the delamination front and on the size of the load step [13–15]. On the other hand, the cohesive zone model-based elements have the advantage, when compared to the virtual crack closure technique-based elements, of being almost independent on the mesh and on the time step. Cohesive elements are characterized by a traction-separation law, based on quasi-arbitrary and empirical parameters [16–19], which need an accurate calibration, from experimental tests, to obtain reliable numerical solutions [20]. The main focus of this paper is to establish a robust numerical-experimental procedure to correctly set the cohesive element parameters. A bilinear traction-separation law is used to define the cohesive mechanical behaviour. A first linear-elastic law defines the stiffness of the cohesive interface up to the damage onset, followed by a progressive stiffness reduction, up to the complete failure. The parameters involved in the definition of the traction-separation law are the cohesive element

penalty stiffness  $K$ , the interfacial strength, which is the damage onset stress, and the fracture toughness. These parameters can be found by means of three-point bending (3PB), double cantilever beam (DCB), and end-notched flexure (ENF) mechanical tests, correlated to numerical analyses. Finally, a first preliminary validation of the proposed procedure has been carried out thanks to numerical-experimental comparisons.

## 2. Theoretical Background

The cohesive zone models represent one of the most evolved theories in the area of fracture mechanics. These models are largely used to simulate crack onset and evolution in solids.

Using the cohesive approach, the formation of fractures is considered as a gradual phenomenon in which the separation of surfaces, involved by the crack, occurs through an extension of the crack tip, or cohesive area, and is counteracted by cohesive tractions.

Indeed, the elements introduced in the cohesive zone are not representative of a physical layer, but they are simply representative of the cohesive forces occurring when the crack advances. For this reason, in order to simulate interlaminar damage between two adjacent plies (delamination), the cohesive elements are placed, as shown in Figure 1(a), in the interface area between the elements of the two consecutive plies.

CZM-based elements are governed by a law linking the variation of the tensile force acting on the connected surfaces ( $\sigma$ ) to their separation ( $\delta$ ). This relation can be represented by a curve called traction ( $\sigma$ )-separation ( $\delta$ ) curve (Figure 1(b)).

The area underneath the curve is representative of the energy required for the separation, i.e., the fracture energy  $G_c$ . The segment OA is representative of an initial step in which the material is considered undamaged. Then, the point A identifies the onset of the damage. The coordinates of point A are predicted by means of the ‘‘quadratic nominal stress’’ criterion (QUADS), introduced in the following equation:

$$\left(\frac{\langle\sigma_n\rangle}{N_{\max}}\right)^2 + \left(\frac{\sigma_t}{T_{\max}}\right)^2 + \left(\frac{\sigma_s}{S_{\max}}\right)^2 = 1. \quad (1)$$

According to this criterion, a combination of nominal and allowable stresses in different directions has been used to determine the onset of damage. Indeed,  $N_{\max}$  and  $\sigma_n$  are the allowable and the nominal stresses in the pure normal mode,  $T_{\max}$  and  $\sigma_t$  are the allowable and the nominal stresses in the first shear direction, and  $S_{\max}$  and  $\sigma_s$  are the allowable and the nominal stresses in the second shear direction.

Finally, the damage evolution is described by the descending segment of the traction-separation curve (AC). The law adopted to represent this behaviour, which is based on the energy dissipated during the damage process, is the ‘‘power law’’ criterion reported in the following equation:

$$\left(\frac{G_I}{G_{Ic}}\right)^\alpha + \left(\frac{G_{II}}{G_{IIc}}\right)^\alpha + \left(\frac{G_{III}}{G_{IIIc}}\right)^\alpha = 1. \quad (2)$$

In equation 2,  $G_I$ ,  $G_{II}$ , and,  $G_{III}$  are, respectively, the energy release rates related to the fracture modes I, II, and III. These values of the energy release rate are calculated by the numerical software evaluating the displacement and stress of the nodes for each fracture mode. The experimental coefficient  $\alpha$  can be assumed between 1 and 1.6. In the frame of the present work, it is assumed to be 1.

The energy  $G_{jc}$  dissipated due to the damage has been calculated by using numerical-experimental correlations between the experimental data from three-point bending (3PB) tests, double cantilever beam (DCB) tests, and end-notched flexure (ENF) tests, and the corresponding numerical results performed in this work.

## 3. Cohesive Zone Model

The cohesive zone model is characterized by 9 different parameters:

- (i) Penalty stiffness:  $k_{nn}$ ,  $k_{ss}$ , and  $k_{tt}$
- (ii) Initial failure parameters:  $N_{\max}$ ,  $S_{\max}$ , and  $T_{\max}$
- (iii) Fracture toughness:  $G_{Ic}$ ,  $G_{IIc}$  (first shear direction), and  $G_{IIIc}$  (second shear direction)

These parameters can be reduced to 6, assuming  $k_{ss} = k_{tt}$ ,  $S_{\max} = T_{\max}$ , and  $G_{IIc} = G_{IIIc}$

In the following paragraphs, a numerical-experimental methodology for characterising the mechanical properties of the cohesive layer is presented.

The procedure is divided into three main steps. Each step is aimed at defining a parameter representative of the cohesive behaviour:

- (i) Step 1: definition of cohesive stiffness using the 3PB tests as reference data
- (ii) Step 2: definition of normal and shear strength using DCB and ENF tests as reference data
- (iii) Step 3: definition of fracture toughness using DCB and ENF tests as reference data

Figure 2 shows, schematically, how the final traction-separation curve is build up step by step.

### 3.1. Penalty Stiffness Definition: Three-Point Bending Test.

An appropriate definition of the cohesive element penalty stiffness is mandatory to accurately predict the structural response of composite parts. Indeed, high cohesive penalty stiffness induces an early damage onset and a too large postfailure phase (and relative softening). On the other hand, if the penalty stiffness is too low, cohesive elements will deform, resulting in a significant relative sliding and/or penetration between nodes at the interface. According to some authors [21–28], the penalty stiffness could be defined as a function of the interface thickness,  $t_{coh}$ , and elastic moduli of the interface ( $E_3$ ,  $G_{13}$ , and  $G_{23}$ ), as described in the following equation:

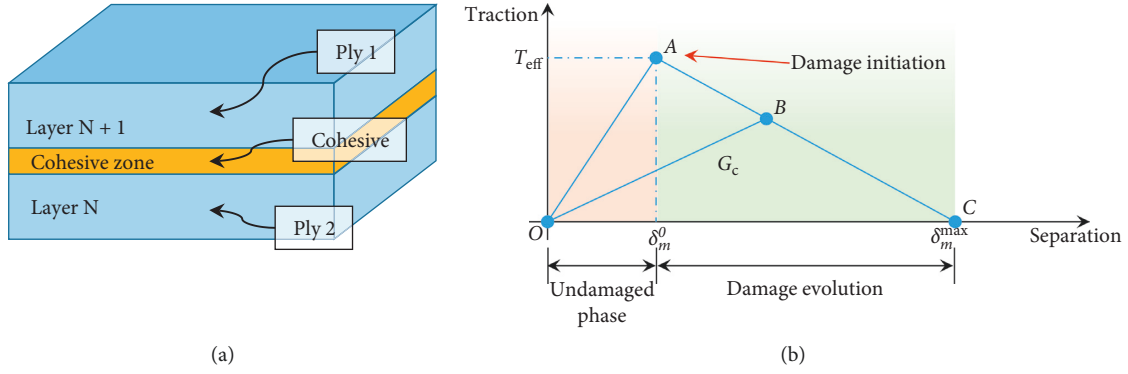


FIGURE 1: (a) Location of the cohesive elements between adjacent layers and (b) traction-separation law.

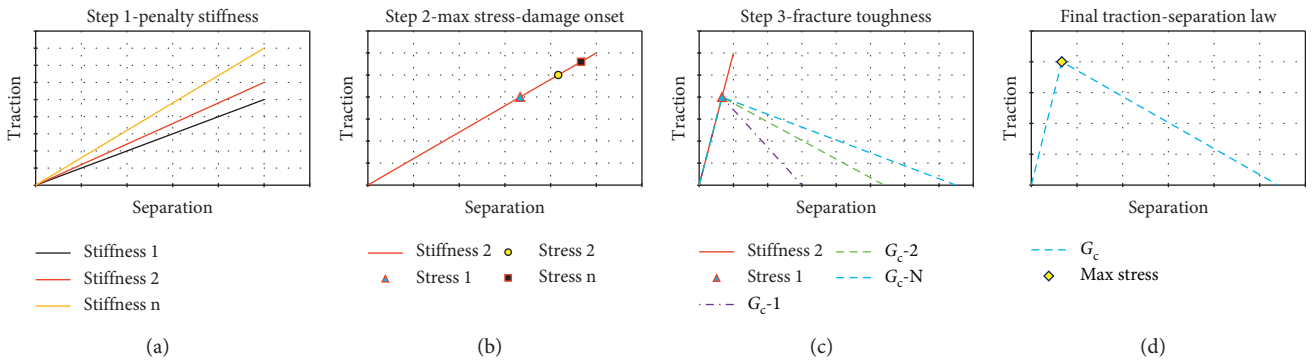


FIGURE 2: Definition of traction-separation law, step by step.

$$\begin{aligned}
 k_{nn} &= \frac{E_3}{t_{coh}}, \\
 k_{ss} &= \frac{G_{13}}{t_{coh}}, \\
 k_{tt} &= \frac{G_{23}}{t_{coh}}.
 \end{aligned} \quad (3)$$

In this work, zero thickness cohesive elements have been considered. Hence, the penalty stiffness has been determined by means of a three-point bending test.

The properties of the adopted material system are reported in Table 1, while the geometrical properties are listed in Table 2.

According to Table 2,  $a$  indicates the specimen span length that is supported,  $b$  the specimen width,  $L$  the specimen length,  $h$  its total thickness, and  $t_{ply}$  the nominal thickness of each ply. The number of plies of the whole laminate is 24, while the stacking sequence is  $[45^\circ, -45^\circ, 0^\circ, 90^\circ]_{3S}$ . The supports and the loading rollers have been modelled by means of three 5 mm radius cylinders.

Two numerical models have been considered: the first one has been discretized by means of *SC8R* continuum shell elements with a reduced integration scheme (CS), while *C3D8I* solid elements (SD), with incompatible mode option, have been used for the second one. Both the numerical models have been discretized by introducing one element

TABLE 1: Material properties for 3PB test.

Material properties				
$E_{11}$ (MPa)	$E_{22}$ (MPa)	$G_{12}$ (MPa)	$\nu_{12}$	Ply thickness (mm)
140000	7930	3900	0.31	0.187

TABLE 2: Geometry data for 3PB test.

Geometrical properties					
$L$ (mm)	$a$ (mm)	$b$ (mm)	$h$ (mm)	$r$ (mm)	$t_{ply}$ (mm)
100	80	4.53	4.45	5	0.186

per ply through the thickness. A 4 mm displacement has been applied on the loading cylinders.

The numerical models have been validated through experimental data comparison, in terms of load as a function of the applied displacement. The experimental tests have been performed in CIRA, using the electromechanical testing system INSTRON 4505 and the standard fixture for three-point bending test. The crosshead rate applied was 0.5 mm/min.

In Figure 3, it is possible to appreciate the good agreement between the numerical stiffness, obtained for both continuum shell (CS) and solid (SD) formulation without cohesive elements, and the experimental ones. Therefore, both element formulations are suitable for this kind of problem, and they can be adopted to describe the

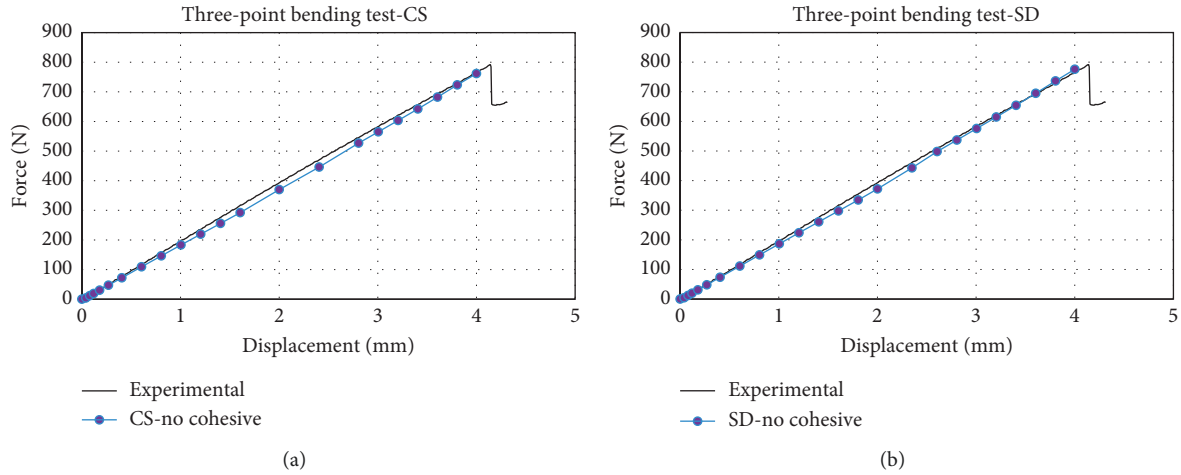


FIGURE 3: 3PB test: experimental-numerical comparison. (a) Continuum shell element and (b) solid elements.

damage behaviour of the specimens according to the analyses reported in the next section.

After the preliminary stage, aimed to the validation of the global stiffness, the cohesive element penalty stiffness has been investigated by inserting a cohesive interface between each ply. In particular, the response of the structure, varying the penalty stiffness of each one of three different fracture modes, has been assessed.

**3.1.1. Normal Direction.** The first set of analyses has been focused on the effects of variation of the parameter  $k_{nn}$  (normal stiffness). According to the analyses, low values of  $k_{nn}$  result in the interpenetration between adjacent plies located in the region below the loading cylinders, while the external sides of the structure, which are loaded in tension (thought the thickness), will experience the separation between the adjacent plies.

Furthermore, low values of  $k_{nn}$  can promote numerical errors related to the computer precision. The optimum value needs to be high enough to correctly represent the mechanical behaviour of the cohesive element, avoiding effects like surface interpenetration and/or separations between adjacent plies or, at least, making them negligible. Moreover, it should not be too high, in order to avoid a premature failure onset and the following increasing of the postfailure regime.

For a complete analysis of the parameters representing the stiffness of the cohesive layers, the parameters have been reported in logarithmic scale. Hence, the parameters  $SFK_n$ ,  $SFK_s$ , and  $SFK_t$ , have been used to scale, respectively, the parameters  $k_{nn}$ ,  $k_{ss}$ , and  $k_{tt}$  in the logarithmic graph.

Figures 4 and 5 show that values of  $SFK_n$  equal to 10 or higher result in low penetration. Therefore, in this work, the interpenetration has been assumed negligible for  $SFK_n = 10$ . The ply thickness is in the order of  $10^{-1}$  mm, and thus, it was considered acceptable to set the threshold of the interpenetration in the order of  $10^{-3}$  mm.

**3.1.2. First Shear Direction.** The second set of analyses has been focused on the  $k_{ss}$  parameter, which influences the

sliding between adjacent plies along the  $X$ -axis, as shown in Figure 6. The figure shows a very clear and widespread sliding among all plies.

Also in this case, several analyses have been performed by varying the  $SFK_s$  parameter and evaluating both the sliding (along the  $X$ -axis) and the global stiffness of the model.

According to Figures 7 and 8 for both the CS and the SD models, for  $SFK_s = 10$ , the maximum sliding value along  $x$  is about  $10^{-3}$  mm, hence negligible according to the considerations on the threshold drawn in the previous section.

**3.1.3. Second Shear Direction.** This third and last set of analyses has been focused on the  $k_{tt}$  parameter, which influences the sliding between adjacent plies along the  $Y$ -axis, as shown in Figure 9. Also in this case, the figure shows a very clear and widespread sliding, and in the same image, some ply interfaces are highlighted.

This last set of analyses has been performed by varying the  $SFK_t$  parameter and evaluating both the sliding (along the  $Y$ -axis) and the global stiffness of the model.

From Figures 10 and 11, for both the CS and the SD models, the value of  $k_{tt}$  has been found not influencing in a significant way the relative displacements at interfaces. For this reason, cohesive penalty stiffness values have been set as  $SFK_{n,s,t} = 10$ .

In Tables 3 and 4, the results obtained for both the discretized models (continuum shells and solid elements) are summarised.

The next subsection focuses on the parameters of cohesive elements governing the failure initiation and evolution.

**3.2. Cohesive Strength Definition.** In this subsection, cohesive interfacial strengths are investigated. These values represent the stresses at the interface between two adjacent plies, which influence the onset of an interlaminar damage. A numerical-experimental correlation based on DCB and ENF tests has been performed in order to determine the

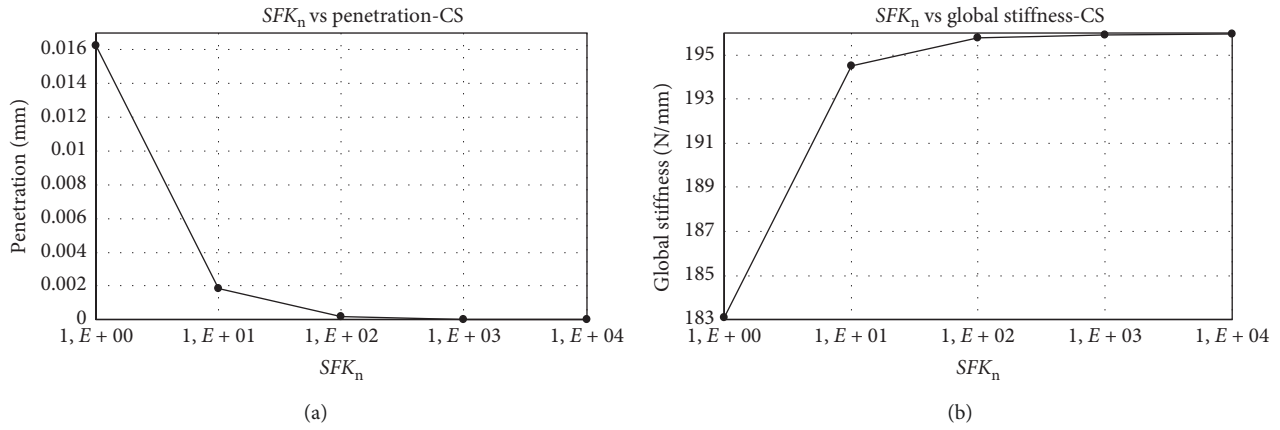


FIGURE 4: Penetration (a) and global stiffness (b) as a function of  $k_{nn}$  (CS model).

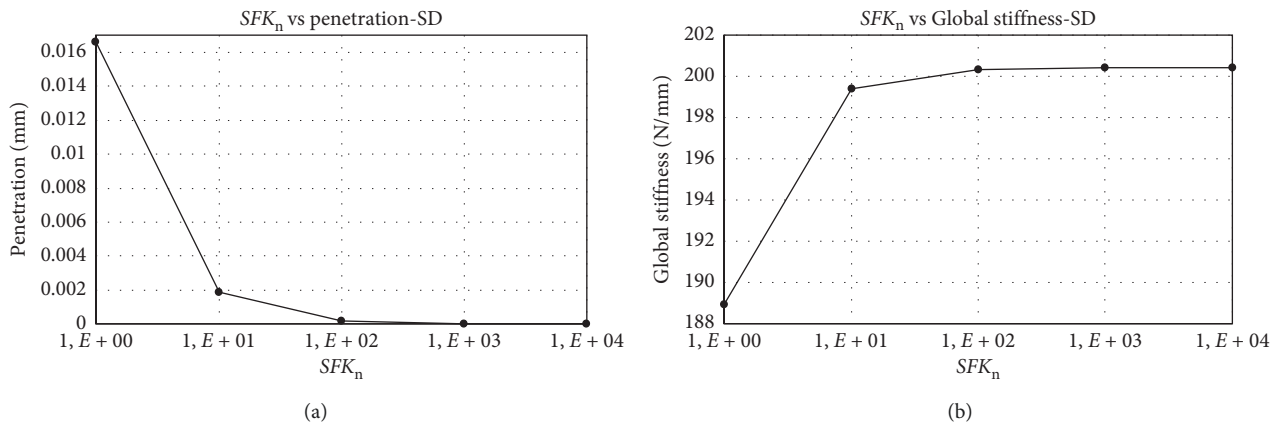


FIGURE 5: Penetration (a) and global stiffness (b) as a function of  $k_{nn}$  (SD model).

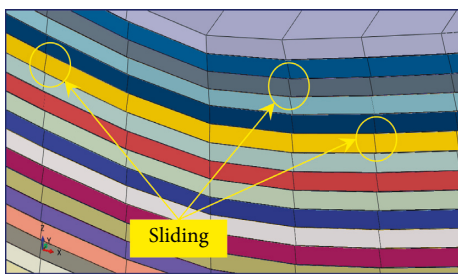


FIGURE 6: Sliding between adjacent plies along x direction.

cohesive element interface strength for each damage mode. All experimental tests have been performed in CIRA, using the electromechanical testing system INSTRON 4505 and the standard fixture as requested by correlated test specifications.

**3.2.1. Normal Strength Definition: Double Cantilever Beam Test.** According to the experimental test procedure ASTM D5528 [29], the average value of 0.288 N/mm has been found for the Mode I interlaminar fracture toughness (10 specimens have been tested). In this phase, the cohesive element

interfacial opening strength is set by means of a numerical-experimental correlation based on a DCB test. The investigated specimens are 14-ply unidirectional ( $0^\circ$ ) laminates. The nominal thickness of each ply is 0.186 mm. Figure 12 shows the geometrical dimension of the investigated specimens.

The two loading blocks have been modelled as discrete rigid bodies by means of *R3D4* elements, while the specimen has been modelled by means of *SC8R* elements. MPC tie constrains have been used to bond the loading block on the specimen. The specimen is divided, ideally, into two sublaminates (the upper and the lower one). Between the two sublaminates, the debonding region has been modelled by using cohesive surfaces and cohesive elements, both based on the traction-separation law. A 10 mm opening displacement has been imposed. Three different mesh discretizations have been considered for the cohesive interfaces: in particular, 4 mm, 2 mm, and 1 mm elements have been used. Besides, the effect of the viscous regularization on the different models has been assessed as well. Indeed, the viscous regularization introduces a fictitious viscosity in the cohesive layer useful to cover convergence difficulties [30]. For such a reason, the different models have been tested with

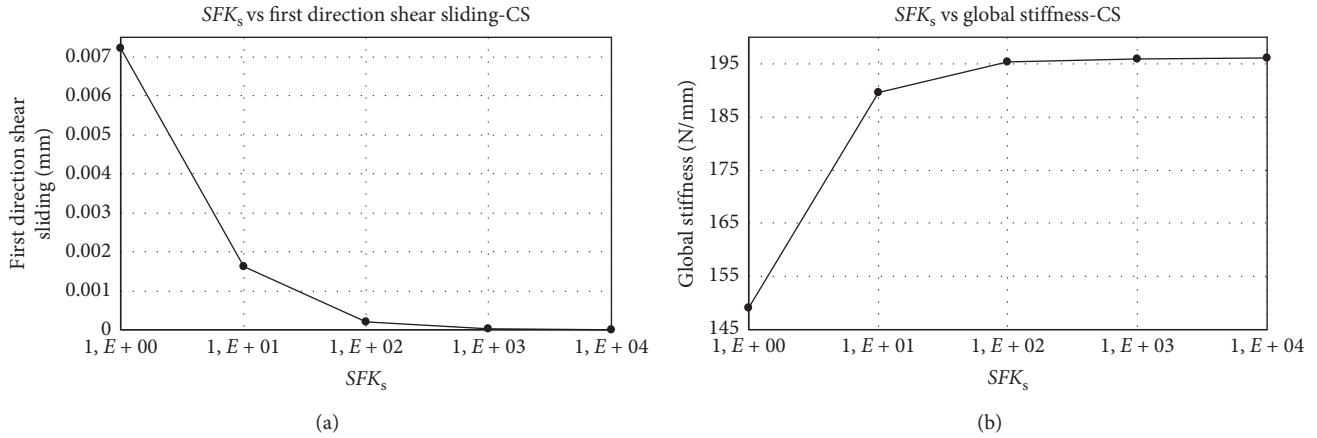


FIGURE 7: Sliding in first shear direction (a) and global stiffness (b) as a function of  $k_{ss}$  (CS model).

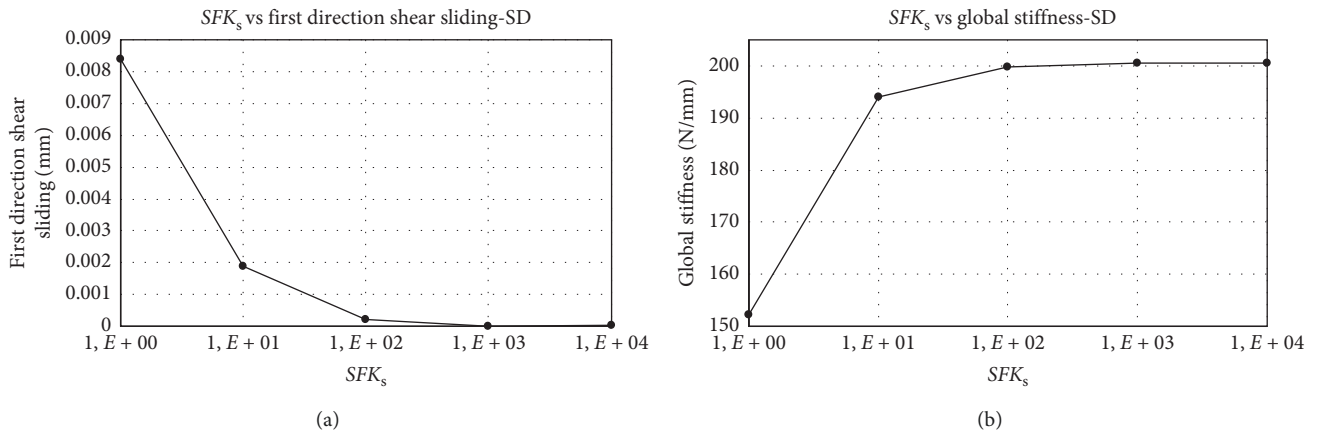


FIGURE 8: Sliding in first shear direction (a) and global stiffness (b) as a function of  $k_{ss}$  (SD model).

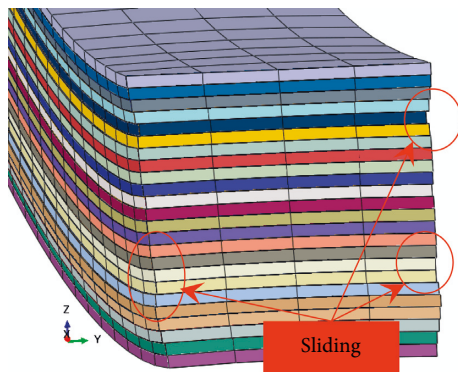


FIGURE 9: Sliding between adjacent plies along  $y$  direction.

a viscous regularization parameter set equal to 0 and to 0.001.

The numerical results, considering the different mesh discretizations, the cohesive models, and the values of the viscous regularization, have been compared to the experimental ones, in terms of load-displacement curve.

For each mesh size, the procedure, aimed at defining the cohesive parameters for the cohesive surface, is divided into

three steps: maximum stress setting, evolution option influence, and viscous stabilization definition.

Therefore, in the first step, the load related to the fracture onset has been found by varying iteratively the parameter  $N_{max}$ . In this first step, the damage evolution and the viscous stabilization have been disabled. In the subsequent second step, the damage evolution has been considered. Finally, in the third step, the effects due to the viscous stabilization have been taken into account. These steps have been performed considering both cohesive element and cohesive interface configurations, for each of the three cohesive interface discretizations. In Figures 13 and 14, the results obtained by considering the mesh size equal to 4 mm are reported.

In Figure 13(a), the experimental results are compared to the numerical ones, adopting the cohesive surface approach and considering different values of  $N_{max}$  parameter and neglecting both the damage evolution option and the viscous stabilization. According to the numerical analyses, the value of  $N_{max}$  which best fits the experimental curve maximum load is  $4.9 \text{ N/mm}^2$ . In Figure 13(b), the experimental results are compared to the numerical ones obtained for  $N_{max} = 4.9 \text{ N/mm}^2$  where, respectively, both evolution and stabilization are neglected, only evolution is considered, and

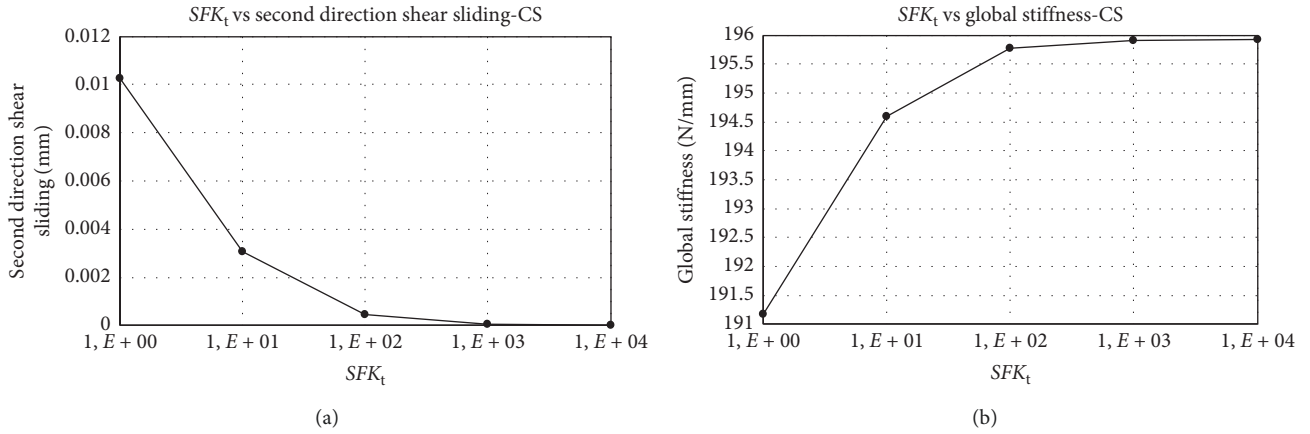


FIGURE 10: Sliding in first shear direction (a) and global stiffness (b) as a function of  $k_{tt}$  (CS model).

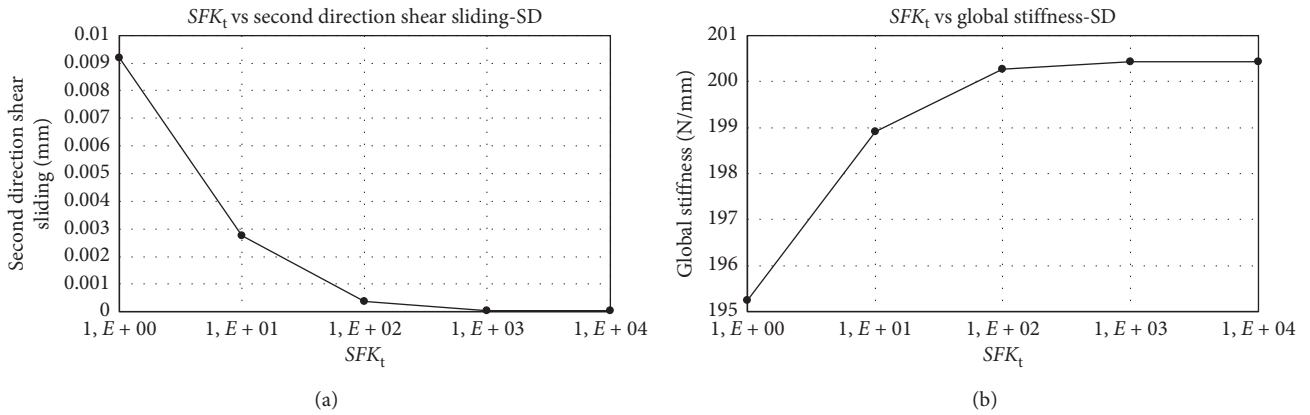


FIGURE 11: Sliding in first shear direction (a) and global stiffness (b) as a function of  $k_{tt}$  (SD model).

TABLE 3: Summary of three-point bending numerical test results (CS model).

Numerical three-point bending test (continuum shell)	$SFK_n = 10$	$SFK_s = 10$	$SFK_t = 10$
Penetration (mm)	$1.880E-03$	$2.000E-05$	$2.000E-05$
First direction shear sliding (mm)	$2.330E-05$	$1.619E-03$	$2.330E-05$
Second direction shear sliding (mm)	$4.611E-05$	$4.611E-05$	$3.057E-03$
Global stiffness (N/mm)	194.4	189.5	194.6

TABLE 4: Summary of three-point bending numerical test results (SD model).

Numerical three-point bending test (solid element)	$SFK_n = 10$	$SFK_s = 10$	$SFK_t = 10$
Penetration (mm)	$1.890E-03$	$2.000E-05$	$2.000E-05$
First direction shear sliding (mm)	$2.510E-05$	$1.902E-03$	$2.510E-05$
Second direction shear sliding (mm)	$3.872E-05$	$3.872E-05$	$2.746E-03$
Global stiffness (N/mm)	199.41	194.00	198.91

both evolution and stabilization are considered. According to Figure 13(b), the viscosity stabilization increases the peak load. Hence, the use of large values of the stabilization parameter can cause a toughening of the material response. Moreover, it can produce a stable propagation of delamination in the case of unstable delamination growth.

Figure 14 shows the results obtained by considering cohesive elements instead of cohesive surfaces. According to

Figure 14, the delamination onset occurs for a smaller load, compared to the experimental one. However, both the models show a final peak load very close to the experimental one. Finally, the cohesive element approach seems to be less influenced by the viscosity stabilization parameter.

In particular, Figure 15(a) shows a comparison between the experimental and numerical results obtained using the cohesive surface approach. The numerical results have been

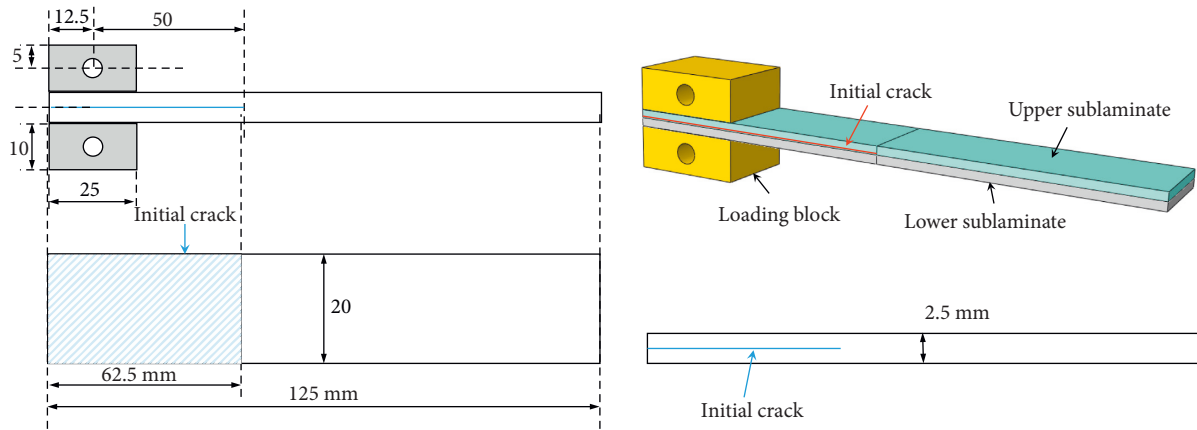


FIGURE 12: DCB: specimen data.

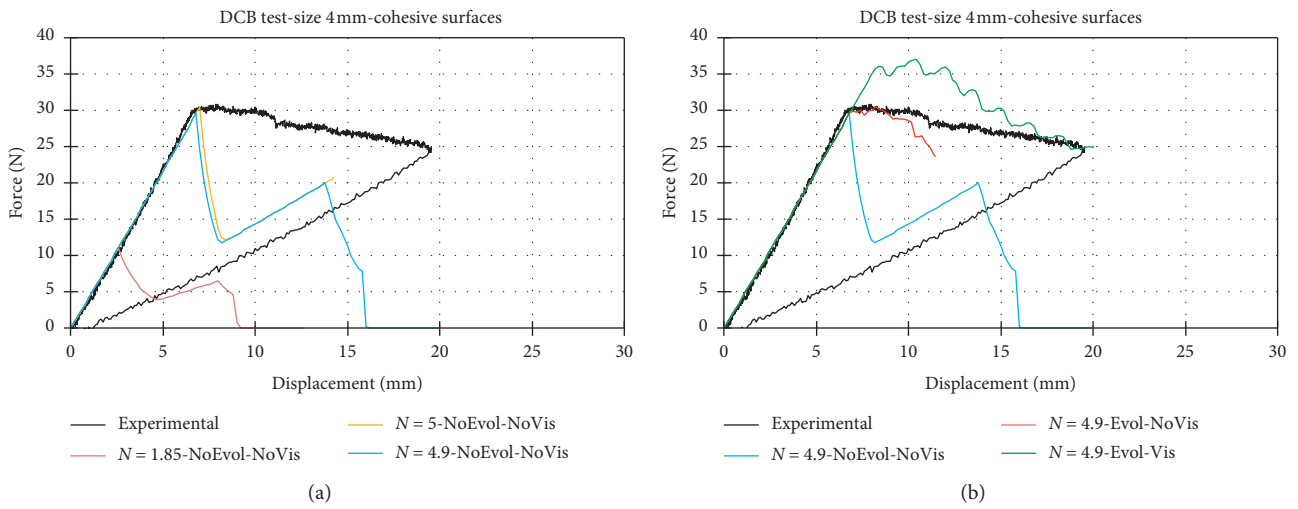


FIGURE 13: DCB test: cohesive surface approach (element size 4 mm).

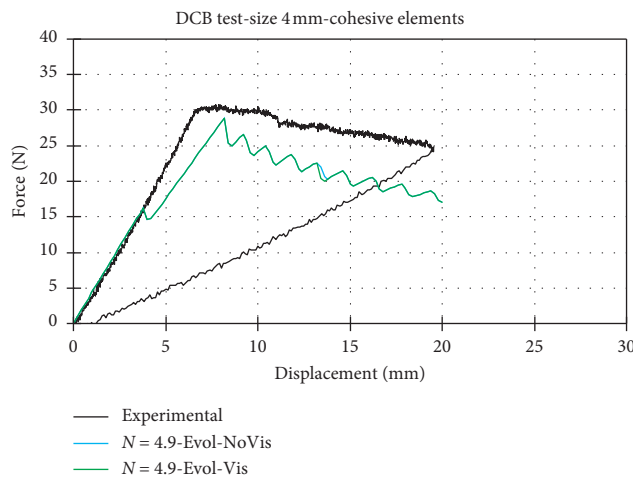


FIGURE 14: DCB test: cohesive element approach (element size 4 mm).

obtained by varying the  $N_{max}$  parameter and disabling the damage evolution option and thus neglected the viscous stabilization. Moreover, Figure 15(a) shows that the best fit

of the numerical-experimental curves is obtained for a value of  $N_{max}$  equal to  $12 \text{ N/mm}^2$ . In Figure 15(b), the different numerical results, obtained for  $N_{max} = 12 \text{ N/mm}^2$  and by



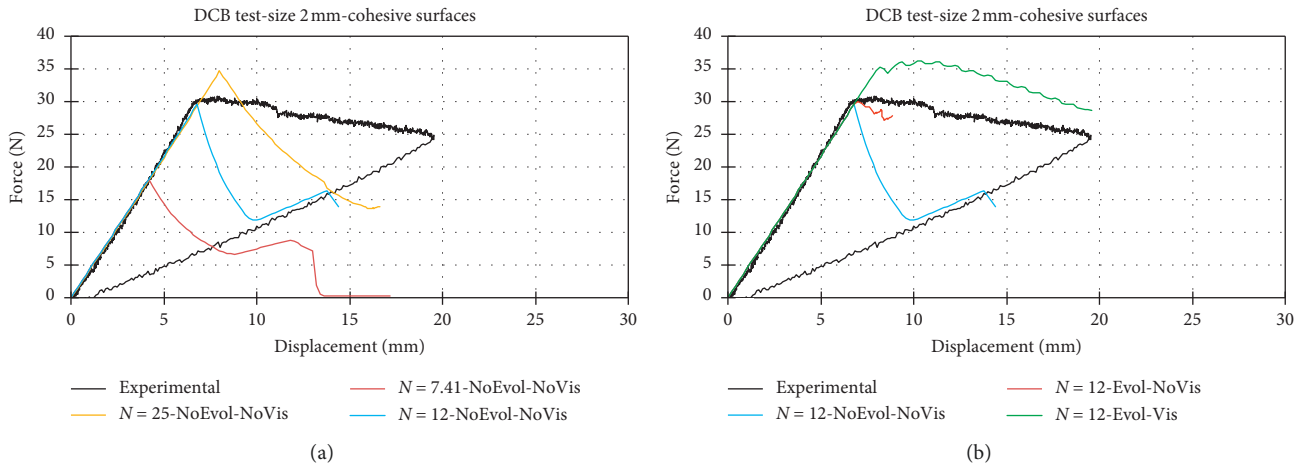


FIGURE 15: DCB test: cohesive surface approach (element size 2 mm).

neglecting both evolution and stabilization, considering only evolution, and considering both evolution and stabilization, are compared with the experimental ones. The same considerations made for the model with 4 mm cohesive element size can be repeated for the model with 2 mm cohesive element size.

Finally, Figure 16 shows the results of the cohesive element model.

In Figures 15 and 16 the results obtained by considering 2 mm element size are reported.

According to Figure 16, the delamination onset occurs for a lower load compared to the experimental one. However, both the models show a final peak load very close to the experimental one.

In Figures 17 and 18, the results obtained by considering the mesh size equal to 1 mm are introduced.

In Figure 17, the experimental results are compared to the cohesive surface numerical ones, obtained by neglecting both the damage evolution and the viscous stabilization for different values of  $N_{\max}$ . The best numerical results have been obtained considering  $N_{\max} = 25 \text{ N/mm}^2$ . As for the 4 mm and 2 mm mesh size models, damage evolution and viscous stabilization influence the model response, as shown in Figure 17.

According to Figure 18, a similar behaviour is obtained for the cohesive surface and cohesive element models, considering the same interfacial opening strength. Moreover, the resulting load-displacement curve is in good agreement with the one obtained from the cohesive surfaces by neglecting the viscous stabilization.

Finally, Figure 19 compares the deformed shapes of the experimental and numerical results corresponding to the most accurate numerical parameter set.

**3.2.2. Transverse Strength Definition: End-Notched Flexure Test.** According to the experimental test procedure prEN 6034 [31], several tests have been performed in order to evaluate the Mode II fracture toughness. The experimental mean value, considering the 10 tested specimens, is equal to

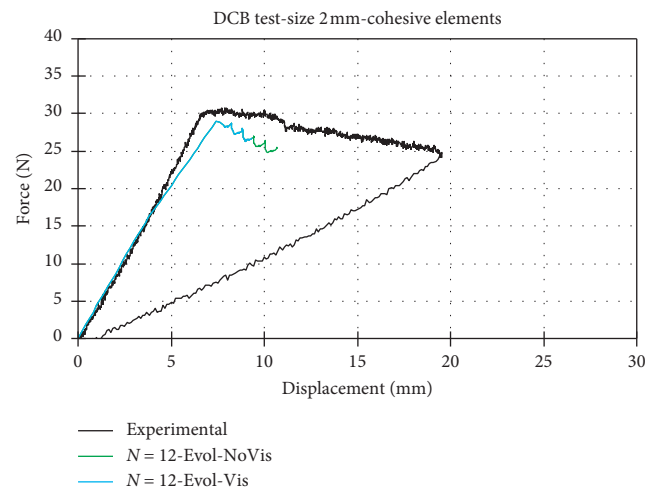


FIGURE 16: DCB test: cohesive element approach (element size 2 mm).

0.610 N/mm. Here, a numerical analysis representing the end-notched flexure test is performed. The numerical results are then compared to the experimental ones to set the transverse strength interface parameters to be adopted by both cohesive surface and cohesive element approaches.

As for the DCB test, different models have been used to simulate the ENF test. For all the models, continuum shell SC8R elements with a reduced integration scheme have been used. A discretization of one element per sublaminar along the thickness has been adopted. Crack propagation has been modelled again by using two different techniques: cohesive surfaces and cohesive elements.

The investigated specimens are 14-ply unidirectional ( $0^\circ$ ) laminates. The nominal thickness of each ply is 0.186 mm. The specimen dimensions are reported in Figure 20.

The supports and the loading nose, shown in Figure 20, have been modelled as discrete rigid bodies by using R3D4 elements. The support radius is 5 mm, while the loading nose radius is equal to 6.25 mm. The lower supports have been fixed, while a 10 mm displacement has been applied on the

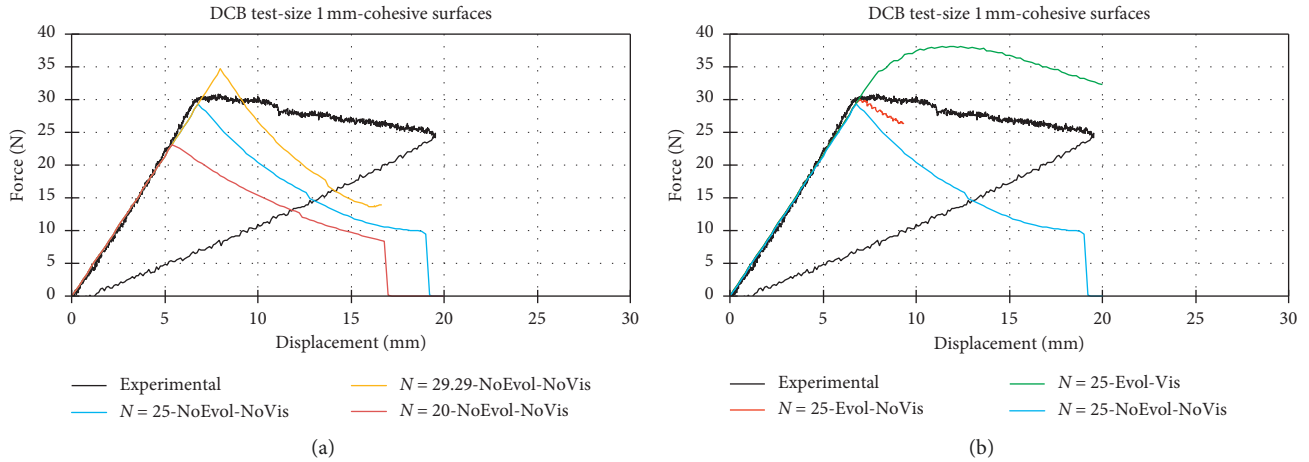


FIGURE 17: DCB test: cohesive surface approach (element size 1 mm).

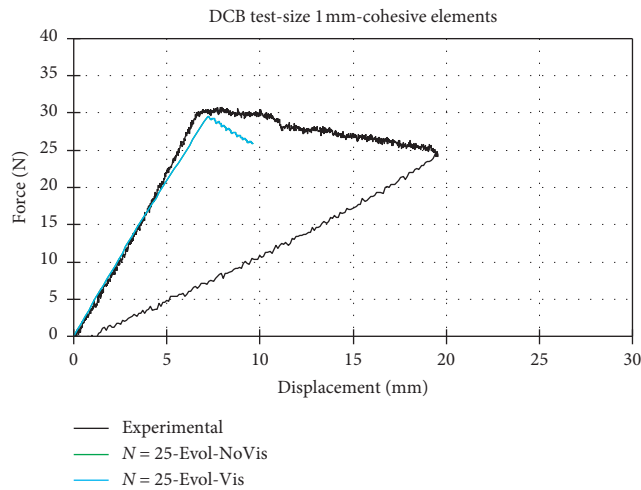


FIGURE 18: DCB test: cohesive elements (element size 1 mm)—damage evolution.

loading nose in the laminate thickness direction. The strategy adopted to evaluate the interfacial shear strength is the same that the one adopted in the DCB test.

In Figures 21 and 22, the results obtained with 4 mm element size are reported.

From the Figures 21 and 22, it is possible to notice that for a value  $S_{\max} = 45 \text{ N/mm}^2$ , the numerical results are in good agreement with the experimental ones with damage evolution and with no viscosity by adopting 4 mm cohesive elements instead of cohesive surfaces. Since the delamination growth in the ENF test is quite fast, the load goes down abruptly. Therefore, also the use of no-evolution option provides good results in terms of postfailure (delamination growth) behaviour. The most accurate results are obtained by considering the evaluation without viscous stabilization, which led to a more sudden delamination growth.

The cohesive element approach seems to be less influenced by the viscous stabilization and thus gives good results using both parameters.

In Figures 23 and 24, the results obtained with 2 mm element size are reported.

According to Figures 23 and 24, it is possible to notice that for a value  $S_{\max} = 80 \text{ N/mm}^2$  the numerical results are in good agreement with the experimental ones with damage evolution and with no viscosity by adopting 2 mm cohesive elements instead of cohesive surfaces.

Also for a mesh size equal to 2 mm, the two numerical curves are very similar, meaning that the numerical results are minimally influenced by the viscous stabilization when the cohesive element approach is adopted.

Unfortunately, the ENF model with 1 mm element size presented convergence problems when no damage evolution was specified; for this reason, the approach above presented could not be applied. In this case, the approach followed is to directly model delamination with damage evolution and a viscosity coefficient of 0.0001 in order to not influence the model response significantly and try the interfacial shear strength values which give the best load-displacement curve compared to the experimental data. In Figure 25, the results

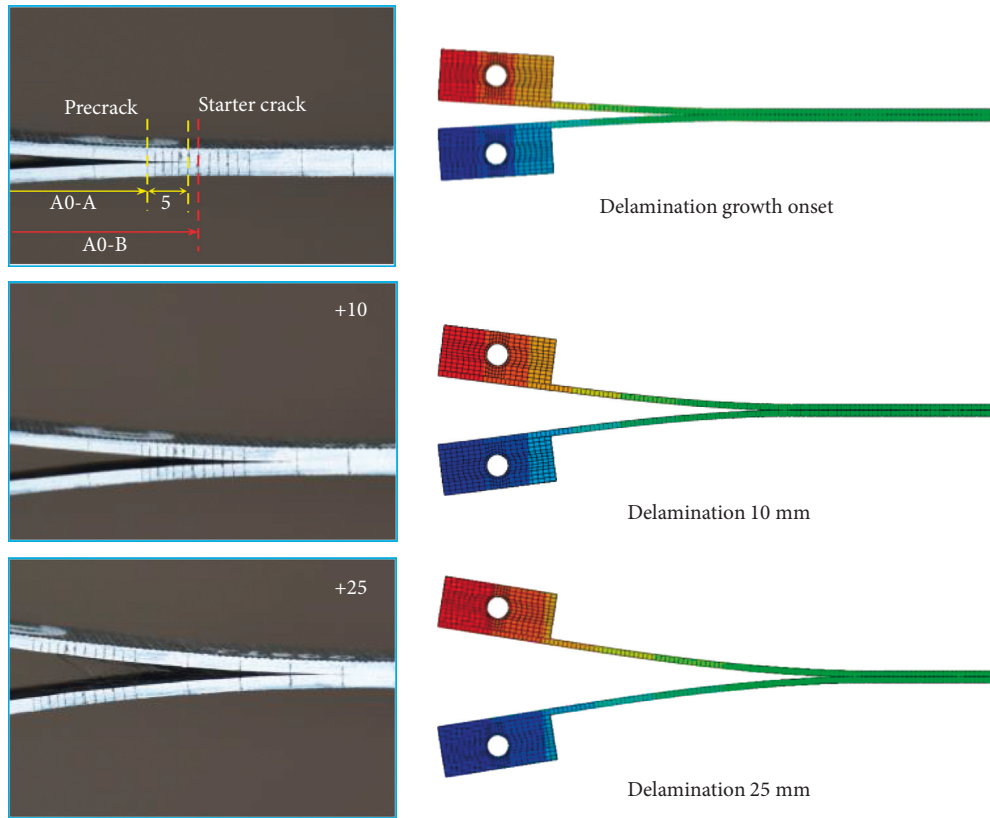


FIGURE 19: DCB: experimental and numerical deformed shape.

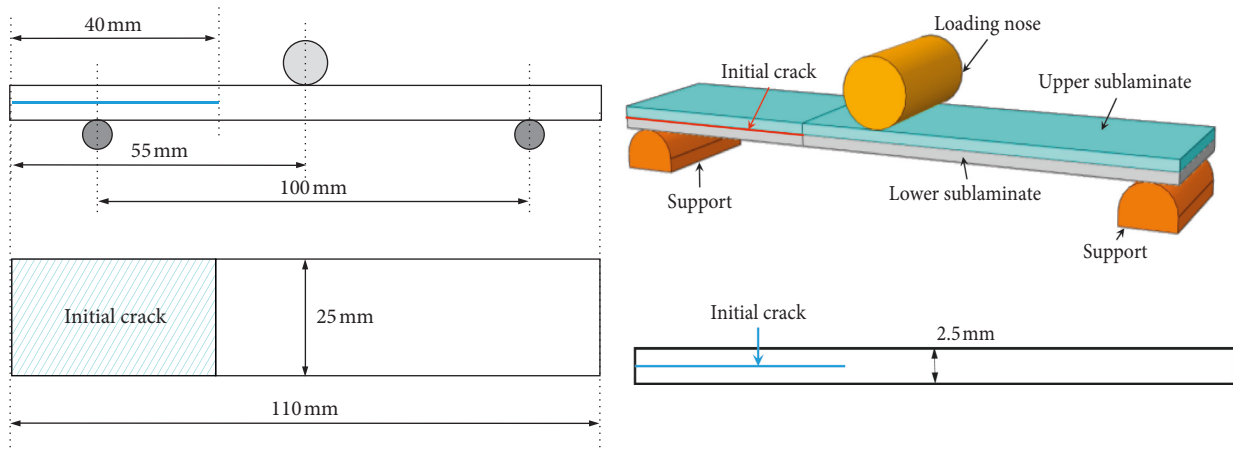


FIGURE 20: ENF: geometrical description.

obtained for 1 mm element size are introduced, using the cohesive surface and cohesive element approach.

According to Figure 25, it is possible to notice that for a value  $S_{max} = 110 \text{ N/mm}^2$ , the numerical results are in good agreement with the experimental ones with damage evolution and with no viscosity by adopting 1 mm cohesive elements instead of cohesive surfaces. Reducing up to 1 mm the element size, unfortunately, leads to convergence problem for all models, and further, it does not produce an improvement on the quality of the results.

Finally, in Figure 26, the experimental deformed shape is compared with the numerical predicted one, corresponding

to the numerical model with the most accurate parameter set.

3.2.3. *Results Summary.* In Table 5, a summary of the fracture toughness, evaluated by means of the experimental campaign, is reported.  $G_{IIIc}$  has been assumed equal to  $G_{IIc}$ .

In Table 6, a summary of the material interfacial strengths, evaluated by means of the numerical-experimental procedure, is reported.

Finally, the interfacial strengths as a function of the in-plane element size are introduced in Figure 27.

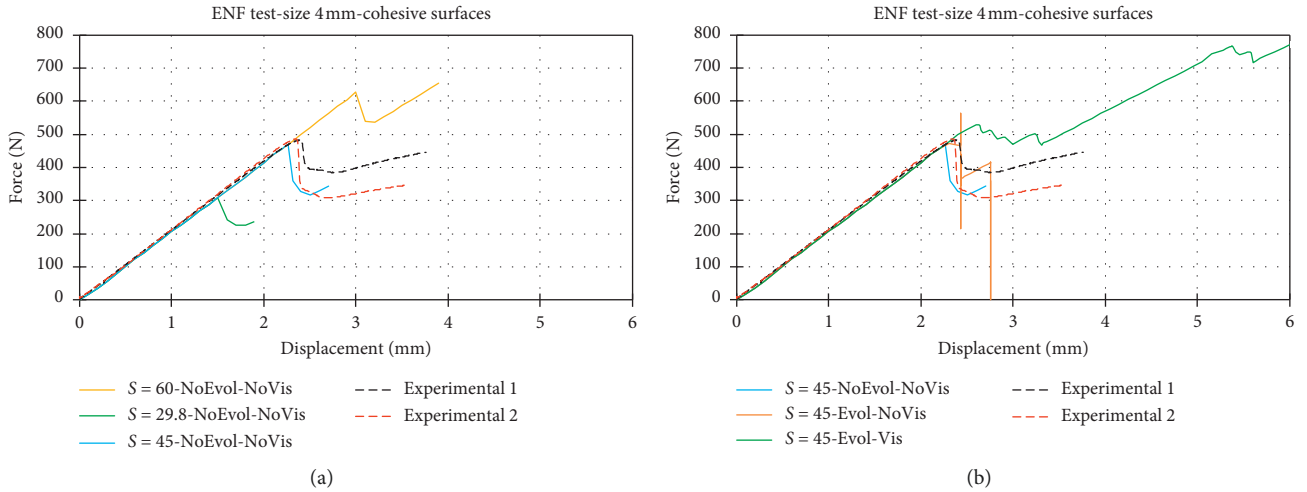


FIGURE 21: ENF test: cohesive surface approach (element size 4 mm).

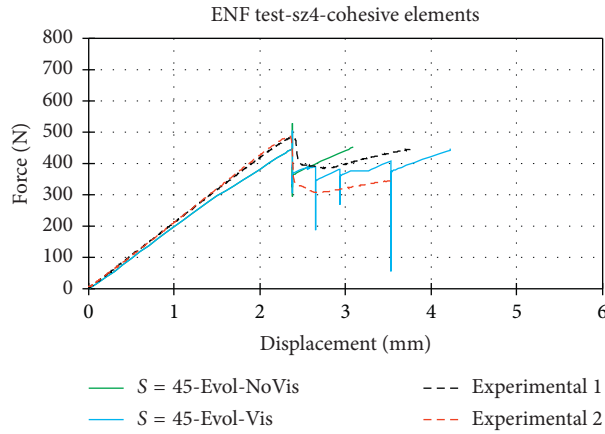


FIGURE 22: ENF test: cohesive element approach (element size 4 mm).

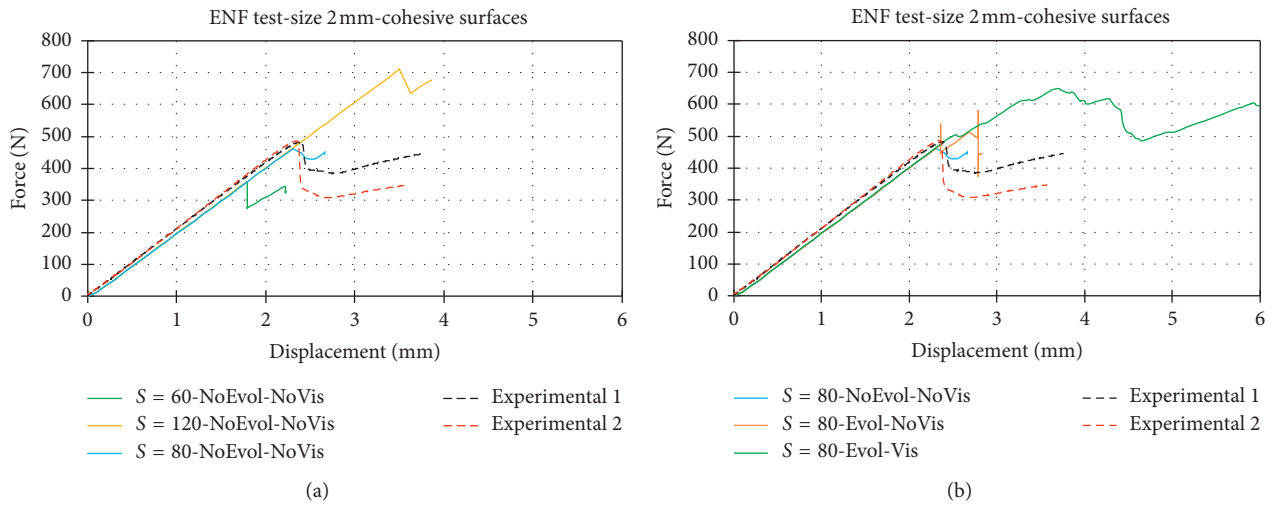


FIGURE 23: ENF test: cohesive surface approach (element size 2 mm).

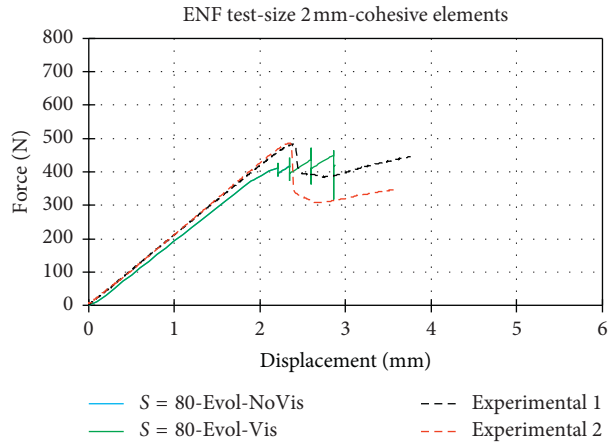


FIGURE 24: ENF test: cohesive element approach (element size 2 mm).

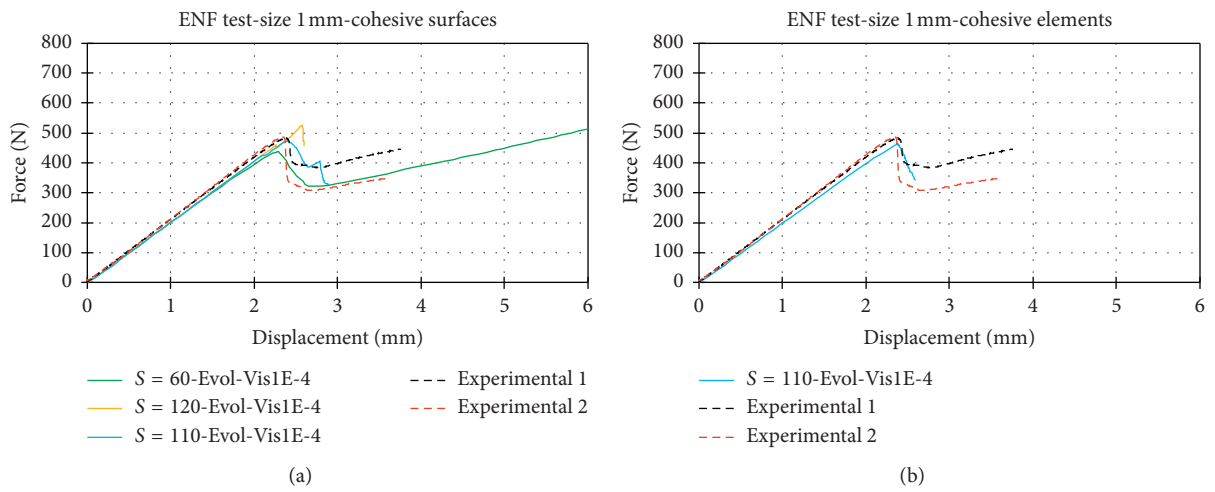


FIGURE 25: ENF test: cohesive elements and surfaces (element size 1 mm).

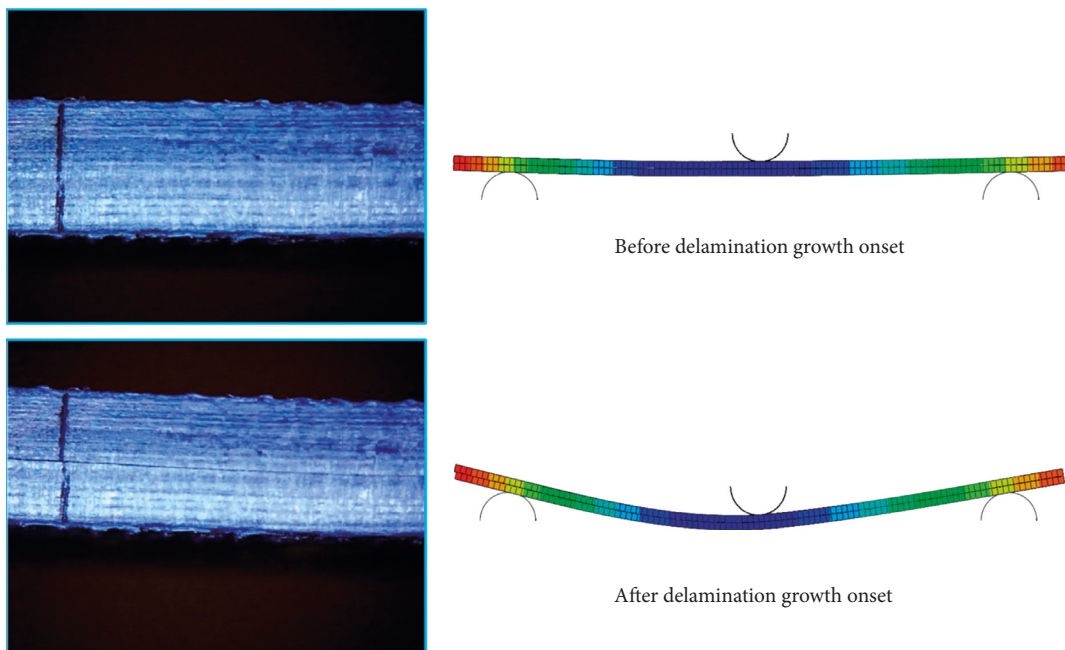


FIGURE 26: ENF: experimental and numerical deformed shape.

TABLE 5: Material fracture toughness.

$G_{Ic}$ (N/mm)	$G_{IIc}$ (N/mm)	$G_{IIIc}$ (N/mm)
0.288	0.61	0.61

TABLE 6: Material interfacial strength.

DCB and ENF tests (continuum shell elements)	$N_{max}$ (N/mm <sup>2</sup> )	$S_{max}$ (N/mm <sup>2</sup> )	$T_{max}$ (N/mm <sup>2</sup> )
Element size 4 mm	4.9	45	45
Element size 2 mm	12	80	80
Element size 1 mm	25	110	110

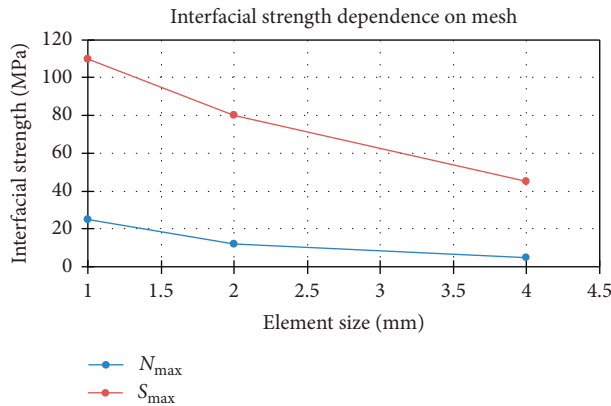


FIGURE 27: Interfacial strength dependence on in-plane element size.

## 4. Conclusions

The main purpose of this work is to present a robust experimental-numerical procedure which is useful to define the cohesive interface parameters to simulate the delamination onset and its evolution, adopting the most used numerical approaches available in the Abaqus FE environment: contact surface with cohesive behaviour option and cohesive elements.

Both approaches require to setting nine parameters in order to correctly simulate the delamination onset and its propagation. These parameters can be divided into three groups, which are related to the structural behaviour, i.e., the stiffness in three directions (normal and the other two orthogonal directions classified as shear directions), to the delamination onset, i.e., the strength of the cohesive layer in three directions (normal and shear strengths), and to the delamination growth, i.e., the fracture toughness energies related to each damage mode. Generally, only the last group is defined by means of experimental tests, while the stiffness and the strength parameters are set according to the matrix properties. Unfortunately, this approach can result in unrealistic results, and thus, in order to have reliable results, it is mandatory to calibrate the numerical models using specific reference data. Furthermore, both procedures (cohesive surface and cohesive elements) are mesh-sensitive; hence, the parameters have to be chosen according to the used

computational mesh. The procedure, here proposed, takes advantage from the results of three types of experimental tests to set all the numerical parameters: three-point bending test, double cantilever beam test, and end-notched flexure test.

In particular, cohesive penalty stiffness has been set by means of experimental three-point bending tests, while the cohesive interfacial strengths and the fracture toughness have been defined by means of experimental double cantilever beam (Mode I) and end-notched flexure tests (Mode II).

The 3PB test allows the introduction of a deformation state which produces both sliding and interpenetration/separation between adjacent plies. Therefore, the test has been used as reference data for numerical analyses focused to define the cohesive stiffness. Ideally, such parameters should be very high, in order to not influence the structural behaviour of the component, but at the same time, very large value leads to convergence issue and an anticipate failure (delamination onset). Therefore, the most suitable values correspond to lower ones which guarantee a reduced sliding and penetration. In this work, the threshold was fixed in the order of  $10^{-3}$  mm that is much lower than the ply thickness (in the order of  $10^{-1}$  mm).

The DCB and ENF tests have been used as reference in order to define the best set of parameters related to the cohesive interface strength and to the fracture toughness ( $G_{Ic}$  and  $G_{IIc}$ ). The numerical analyses have been performed adopting both the cohesive surface and the cohesive element approach. For each approach, several mesh sizes have been considered, in order to highlight the mesh dependency. For each mesh size, it is possible to define the best set of parameters which allow simulating, adequately, the delamination onset and propagation. In particular, the cohesive strength decreases as the mesh size increases. These data represent the stress achieved in the elements along the delamination front, and their sum is equal to the applied load (at any time increments). Since, for a well-defined specimen and material system, the load generating a delamination onset is fixed, the introduction of a higher number of nodes results in the distribution of the same force on a greater number of nodes, thus reducing the force acting on each node.

Both approaches are suitable enough to simulate these kinds of problems. However, the cohesive surface approach is more easy to implement (it is managed as simple contact between bodies) and it is more stable compared to the cohesive element approach. Unfortunately, the delamination growth path depends on the mesh discretization, since any delamination increment is equal to the element size of the plies. Usually, different mesh discretizations can be adopted for the elements of the laminate and the elements of the cohesive layer. However, this option was not considered in this context, and the same discretization has been used for both the composite laminate and the cohesive layer. Therefore, in order to reduce the computational cost, it is possible to define a coarse mesh for the bodies and a finer mesh in the cohesive layer and thus a smoother delamination path.

## Nomenclature

$k_{nn}$ : Cohesive penalty stiffness—pure normal mode  
 $k_{ss}$ : Cohesive penalty stiffness—first shear direction  
 $k_{tt}$ : Cohesive penalty stiffness—second shear direction  
 $SFK_n$ :  $k_{nn}$  scale factor  
 $SFK_s$ :  $k_{ss}$  scale factor  
 $SFK_t$ :  $k_{tt}$  scale factor  
 $\sigma_n$ : Nominal stress—pure normal mode  
 $\sigma_s$ : Nominal stress—first shear direction  
 $\sigma_t$ : Nominal stress—second shear direction  
 $N_{max}$ : Allowable stress—pure normal mode  
 $S_{max}$ : Allowable stress—first shear direction  
 $T_{max}$ : Allowable stress—second shear direction  
 $G_{Ic}$ : Mode I fracture toughness  
 $G_{IIc}$ : Mode II fracture toughness  
 $G_{IIIc}$ : Mode III fracture toughness  
 $t_{coh}$ : Interface thickness.

## Data Availability

No data were used to support this study.

## Conflicts of Interest

The authors declare that there are no conflicts of interest regarding the publication of this paper.

## References

- [1] A. Riccio, G. Di Felice, S. Saputo, and F. Scaramuzzino, "A numerical study on low velocity impact induced damage in stiffened composite panel," *Journal of Computational Simulation and Modeling*, vol. 3, no. 1, pp. 044–047, 2013.
- [2] A. Riccio, R. Cristiano, S. Saputo, and A. Sellitto, "Numerical methodologies for simulating bird-strike on composite wings," *Composite Structures*, vol. 202, pp. 590–602, 2018.
- [3] A. Riccio, G. Di Felice, S. Saputo, and F. Scaramuzzino, "Stacking sequence effects on damage onset in composite laminate subjected to low velocity impact," *Procedia Engineering*, vol. 88, pp. 222–229, 2014.
- [4] A. Sellitto, A. Riccio, A. Russo, M. Zarrelli, C. Toscano, and V. Lopresto, "Compressive behaviour of a damaged omega stiffened panel: damage detection and numerical analysis," *Composite Structures*, vol. 209, pp. 300–316, 2019.
- [5] C. Soutis and P. T. Curtis, "Prediction of the post-impact compressive strength of CFRP laminated composites," *Composites Science and Technology*, vol. 56, no. 6, pp. 677–684, 1996.
- [6] M. R. Wisnom, "The role of delamination in failure of fibre-reinforced composites," *Philosophical Transactions of the Royal Society A: Mathematical, Physical and Engineering Sciences*, vol. 370, no. 1965, pp. 1850–1870, 2012.
- [7] D. J. Elder, R. S. Thomson, M. Q. Nguyen, and M. L. Scott, "Review of delamination predictive methods for low speed impact of composite laminates," *Composite Structures*, vol. 66, no. 1–4, pp. 677–683, 2004.
- [8] T. E. Tay, "Characterization and analysis of delamination fracture in composites: an overview of developments from 1990 to 2001," *Applied Mechanics Reviews*, vol. 56, no. 1, pp. 1–32, 2003.
- [9] M. R. Wisnom, "Modelling discrete failures in composites with interface elements," *Composites Part A: Applied Science and Manufacturing*, vol. 41, no. 7, pp. 795–805, 2010.
- [10] P. Camanho and C. Davila, "Mixed-mode decohesion finite elements for the simulation of delamination in composite materials," NASA/TM-tnqh\_xFFFD;211737, NASA, Washington, DC, USA, 2002.
- [11] F. Aymerich, F. Dore, and P. Priolo, "Simulation of multiple delaminations in impacted cross-ply laminates using a finite element model based on cohesive interface elements," *Composites Science and Technology*, vol. 69, no. 11–12, pp. 1699–1709, 2009.
- [12] A. Riccio, R. Ricchiuto, F. Di Caprio, A. Sellitto, and A. Raimondo, "Numerical investigation of constitutive material models on bonded joints in scarf repaired composite laminates," *Engineering Fracture Mechanics*, vol. 173, pp. 91–106, 2017.
- [13] D. Xie and S. B. Biggers, "Progressive crack growth analysis using interface element based on the virtual crack closure technique," *Finite Elements in Analysis and Design*, vol. 42, no. 11, pp. 977–984, 2006.
- [14] P. F. Liu, S. J. Hou, J. K. Chu et al., "Finite element analysis of postbuckling and delamination of composite laminates using virtual crack closure technique," *Composite Structures*, vol. 93, no. 6, pp. 1549–1560, 2011.
- [15] K. Ronald, "The virtual crack closure technique: history, approach and applications," NASA/CR-2002-211628, ICASE Report No. 2002-10, NASA, Washington, DC, USA, 2002.
- [16] R. D. Borst, J. J. C. Remmers, and A. Needleman, "Mesh-independent discrete numerical representations of cohesive-zone models," *Engineering Fracture Mechanics*, vol. 73, no. 2, pp. 160–177, 2006.
- [17] M. Meo and E. Thieulot, "Delamination modelling in a double cantilever beam," *Composite Structures*, vol. 71, no. 3–4, pp. 429–434, 2005.
- [18] Q. Yang and B. Cox, "Cohesive models for damage evolution in laminated composites," *International Journal of Fracture*, vol. 133, no. 2, pp. 107–137, 2005.
- [19] A. Riccio, S. Saputo, and A. Sellitto, "A user defined material model for the simulation of impact induced damage in composite," *Key Engineering Materials*, vol. 713, pp. 14–17, 2016.
- [20] X. Lu, M. Ridha, B. Y. Chen, V. B. C. Tan, and T. E. Tay, "On cohesive element parameters and delamination modelling," *Engineering Fracture Mechanics*, vol. 206, pp. 278–296, 2019.
- [21] L. Daudeville, O. Allix, and P. Ladevèze, "Delamination analysis by damage mechanics: some applications," *Composites Engineering*, vol. 5, no. 1, pp. 17–24, 1995.
- [22] P. P. Camanho and C. G. Dávila, *Mixed-Mode Decohesion Finite Elements for the Simulation of Delamination in Composite Materials*, National Aeronautics and Space Administration (NASA), Washington, DC, USA, 2002.
- [23] A. Cornec, I. Scheider, and K. H. Schwalbe, *Guidelines for Applying Cohesive Models to the Damage Behaviour of Engineering Materials and Structures*, Springer, Berlin, Germany, 2013.
- [24] I. Scheider, V. Uz, and N. Huber, "Applicability of the cohesive model to fracture of light-weight structures: parameter identification and thickness dependence," in *Proceedings of the 18th European Conference on Fracture: Fracture of Materials and Structures from Micro to Macro Scale*, Dresden, Germany, August 2010.
- [25] R. D. S. G. Campilho, M. F. S. F. de Moura, and J. J. M. S. Domingues, "Using a cohesive damage model to

- predict the tensile behaviour of CFRP single-strap repairs,” *International Journal of Solids and Structures*, vol. 45, no. 5, pp. 1497–1512, 2008.
- [26] R. D. S. G. Campilho, *Strength Prediction of Adhesively-Bonded Joints*, CRC Press, Boca Raton, FL, USA, 2017.
- [27] M. Jung Lee, T. Min Cho, W. Seock Kim, B. Chai Lee, and J. J. Lee, “Determination of cohesive parameters for a mixed-mode cohesive zone model,” *International Journal of Adhesion and Adhesives*, vol. 30, no. 5, pp. 322–328, 2010.
- [28] Y. J. Wang and C. Q. Ru, “Determination of two key parameters of a cohesive zone model for pipeline steels based on uniaxial stress-strain curve,” *Engineering Fracture Mechanics*, vol. 163, pp. 55–65, 2016.
- [29] ASTM International, *ASTM D5528-01 Standard Test Method for Mode I Interlaminar Fracture Toughness of Unidirectional Fiber-Reinforced Polymer Matrix Composites*, ASTM International, West Conshohocken, PA, USA, 2007.
- [30] Simulia, *Abaqus Lectures—Lecture 5: Element-Based Cohesive Behaviour*, Simulia, Johnston, RI, USA, 2019.
- [31] AECMA Standard, *prEN 6034—Aerospace Series Carbon Fibre Reinforced Plastics Test Method Determination of Interlaminar Fracture Toughness Energy Mode II—GIIC*, AECMA Standard, Gulledelle, Bruxelles, Belgium, 1995.





**Hindawi**  
Submit your manuscripts at  
[www.hindawi.com](http://www.hindawi.com)

